

Article

Effects of ErF₃ Particles on the Structure and Physicomechanical Properties of A359 Alloy

Nikolai Kakhidze ^{1,*}, Vladimir Valikhov ¹, Mikhail Selikhovkin ¹, Anton Khrustalyov ¹, Ilya Zhukov ¹,
Sergey Vasiliev ² and Alexander Vorozhtsov ¹

¹ Physics and Technology Faculty, National Research Tomsk State University, 634050 Tomsk, Russia; valihov.snobls@gmail.com (V.V.); mishselikh@gmail.com (M.S.); tofik0014@gmail.com (A.K.); gofra930@gmail.com (I.Z.); abv1953@mail.ru (A.V.)

² State Corporation for Assistance to Development, Production and Export of Advanced Technology Industrial Product «Rostec», 119991 Moscow, Russia; ecamo@mail.ru

* Correspondence: kakhidze.n@yandex.ru

Abstract: In this work, the impact of ErF₃ submicroparticles on the microstructure and mechanical properties of the A359 alloy was studied. ErF₃ particles provided a homogeneous structure in castings produced via the casting method. The modifying effect of ErF₃ particles on the structure of Al–Si alloys is realized through the mechanism of restraining the crystallization front and is achieved through the reduction in the formation of clusters of iron phases and eutectic lamellar silicon. It was found that the addition of 1 wt% ErF₃ to the A359 alloy leads to a decrease in the average grain size by 21% and an increase in the yield strength by 14%, in tensile strength by 16%, in the microhardness of Al₁₅(FeMn)₃Si₂ phase by 34% and in the Al₁₅(FeMnCr)₃Si₂ phase by 7%. The heat treatment of the A359 alloy with ErF₃ particles increased the yield strength by 36% and the tensile strength by 34%. The absence of an effect of ErF₃ particles on the hardness values of the A359 alloy, as well as on the fracture process of the A359 alloy, was observed. The negative influence of ErF₃ particle agglomerates and clusters on the strength characteristics of the investigated alloys was observed. Approaches for further exploring the potential of ErF₃ particles as a strengthening phase in cast aluminum alloys of the Al–Si system were proposed.

Keywords: casting; aluminum; silicon; rare earth elements; erbium; erbium fluoride; dispersion strengthening; heat treatment; structure; strength



Citation: Kakhidze, N.; Valikhov, V.; Selikhovkin, M.; Khrustalyov, A.; Zhukov, I.; Vasiliev, S.; Vorozhtsov, A. Effects of ErF₃ Particles on the Structure and Physicomechanical Properties of A359 Alloy. *Metals* **2023**, *13*, 1463. <https://doi.org/10.3390/met13081463>

Academic Editors: Wenming Jiang, Wenchao Yang and Manoj Gupta

Received: 10 May 2023

Revised: 27 June 2023

Accepted: 4 August 2023

Published: 14 August 2023



Copyright: © 2023 by the authors. Licensee MDPI, Basel, Switzerland. This article is an open access article distributed under the terms and conditions of the Creative Commons Attribution (CC BY) license (<https://creativecommons.org/licenses/by/4.0/>).

1. Introduction

Casting is a versatile method of industrial aluminum production, widely utilizing Al–Si alloys due to their high liquid fluidity and specific strength, coupled with low cost [1]. Despite the advantages of Al–Si alloys, there is a need to enhance the mechanical properties of cast aluminum alloys for weight reduction, increased reliability, and fuel efficiency in the designs of transportation vehicles, including cars and aviation. High mechanical properties in aluminum alloys are achieved through microalloying (up to 0.5 wt%) with scandium, which provides an increase in yield strength of up to 80% and tensile strength of up to 45% [2–4], through the modification of the grain structure [5] and through dispersion strengthening [6]. Due to the high cost of Sc in deformable Al–Mg alloys, its concentration is reduced by adding cheaper Zr [7–13]. However, the combination of Sc and Zr is not effective in Al–Si cast alloys [14], and the modifying effect of Sc is only revealed at high concentrations (up to 1 wt%) as part of it enters the composition of the silicon eutectic and the rest forms the AlSc₂Si₂ phase, which initiates the growth of needle-like iron-rich Al₅FeSi phase [15–17]. Therefore, the addition of 0.4–0.8% Sc increases the yield strength by 8–20% and the ultimate tensile strength by 11–35% in both as-cast and heat-treated conditions [18–20].

Currently, various approaches are being developed for the alloying of Al–Si alloys and other cast aluminum alloys with rare-earth metals (REMs), such as zirconium [21,22], cerium [23], lanthanum [24], and erbium [25–28], with similar mechanisms to scandium that affect the strength properties of aluminum alloys. The most interesting one is the use of erbium due to its market price being 32 times lower than scandium and its ability to form an Al₃Er phase that has similar parameters of a crystal lattice to aluminum [29]. This phase is expected to effectively refine the alloy structure by creating additional crystallization centers. Due to the differences in melting temperatures between aluminum (660 °C) and erbium (1529 °C), master alloys based on aluminum (typical for all REMs) are utilized for erbium’s introduction to alloys. These master alloys are produced via methods, such as the direct alloying or hydriding of REMs [30], using metallic erbium as a raw material. Erbium is found in natural minerals in the form of an oxide [31], which, through an intermediate compound of fluoride or chloride, is synthesized into metallic erbium.

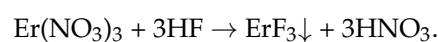
However, it is possible to introduce ex situ micro- and nanoparticles into the metal melt to improve the mechanical properties of Al–Si alloys. Depending on their type and size, such particles can have a modifying [32], strengthening [33,34], or combined [35] effect on the structure and physicomechanical properties of aluminum–silicon alloys. Previous studies have shown positive effects of scandium fluoride particles on the mechanical properties of the A356 alloy [36], including simultaneous increases in yield strength, tensile strength, and ductility. These mechanical behavior characteristics are related to significant differences in physical characteristics (thermal conductivity, electrical conductivity, the coefficient of the thermal linear expansion (CTLE)) between the matrix and strengthening particles. The higher the degree of mismatch between the CTLE coefficients of the particles and matrix, the higher the density of geometrically forced dislocations formed around the particles during alloy crystallization [36]. The formed dislocations contribute to the increase in the strength properties of the alloy due to the entanglement of linear defects and the hindering of their movement under material loading. The CTLE of erbium fluoride ($11 \times 10^{-6} \text{ K}^{-1}$ [37]) is half that of aluminum ($23 \times 10^{-6} \text{ K}^{-1}$ [38]), which can positively affect the mechanical properties of Al–Si alloys. The use of erbium fluoride as a strengthening phase will allow the optimization of the technological process of obtaining high-strength alloys based on Al–Si, since erbium fluoride is an intermediate product in the production of metallic erbium (Figure 1). Thus, the aim of this work is to investigate the effect of erbium fluoride particles on the structure and physicomechanical properties of the aluminum alloy A359.



Figure 1. Two methods of obtaining erbium alloys: alloying using the hydrogenation technology RZM (1–9) or dispersion strengthening with ErF₃ particles (1, 2→5–7→9).

2. Materials and Methods

The production of Al–ErF₃ master alloy. To produce erbium fluoride, an aqueous solution of erbium oxynitride was poured into a solution of hydrofluoric acid (HF) in combination with vigorous stirring.



The resulting solution was washed with distilled water until the pH reached 6–7. The presence of nitrate ions was determined using a qualitative reaction with diphenylamine. Filtration was performed using a vacuum Buchner funnel and a “blue ribbon” filter. The gel-like erbium fluoride was dried in an oven at 70 °C for 12 h, followed by annealing in a furnace at 800 °C for 1 h. The resulting erbium fluoride was loaded into a planetary ball mill with WC balls (3 mm in diameter) at a balls to ErF_3 mass ratio of 3:1. Erbium fluoride was crushed at a frequency of 14 Hz in air for 2 h. An aluminum powder with a purity of 99.7% and an average particle size of 105 μm was added to the ball mill at an Al to ErF_3 ratio of 9:1, along with ceramic balls at the same ratio to obtain a homogeneous mixture of Al– ErF_3 . Mixing was performed at a frequency of 10 Hz for 4 h, followed by sieving through a 150 μm mesh. The resulting mixture was pressed into a mold with a diameter of 13 mm at a pressure of 390 MPa.

The Production of Al–Si– ErF_3 Alloys. The studied alloys were produced by casting into a steel mold followed by heat treatment, according to the regime (*T6*): hardening with incomplete artificial aging. The industrial aluminum alloy A359 (Al 85.1–91.6%; Si 8–11%, Mn 0.2–0.5%; etc.) was used as the starting material for the study. In the experiment, 1.71 kg of the alloy was placed in a graphite–chamotte crucible and melted in a vertical muffle furnace at a temperature of 780 °C with a hold time of 2 h. The crucible with the melt was moved to an open-type furnace to maintain the temperature. After the mechanical removal of slag from the melt surface, Al– ErF_3 master alloy preheated to 200 °C was introduced into the melt, weighing 190 g (amount of 1 wt%). One minute after the introduction of the master alloy, the melt was stirred with an original mixing device [39] for 2 min. The melt at a temperature of 705–720 °C was fed into the gate of the original steel coquille [40] heated to a temperature of 170–190 °C (Figure 2). Two castings of a rectangular cross-section of 100 × 150 × 10 mm were cast from one crucible (the gate and feeder areas were not used in the experiments). The method for obtaining the initial alloy without erbium was similar. For the heat treatment of the obtained alloys, the castings were placed in a muffle furnace heated to 450 °C. After holding for 1 h, the castings were sharply cooled via immersion in water heated to 80 °C. The cooled castings were placed in a furnace heated to 270 °C, incubated for 4 h and cooled together with the furnace.

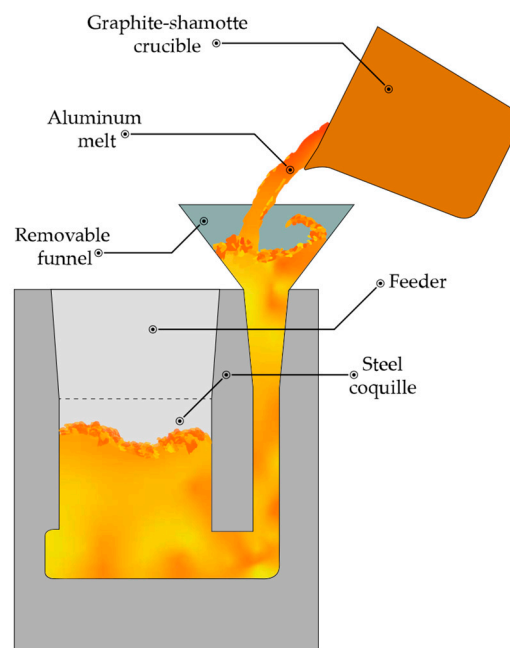


Figure 2. Schematic drawing of the process of the production of the alloys under study by pouring the melt into the steel die casting.

Research methods. The surface morphology of ErF_3 particles was investigated using a scanning electron microscopy (SEM) Quanta 200 3D (the equipment of Tomsk Regional Core Shared (EqTRCS)). The phase composition and structural parameters of powder were studied using X-ray diffraction with a Shimadzu XRD-6000 diffractometer (EqTRCS) in $\text{Cu K}\alpha$ radiation. The quantitative content of phases in the powder was assessed through a full profile Rietveld analysis using the POWDER CELL 2.4 software and the PDF4+ crystal structure database. The chemical composition of the alloys was determined using an iCAP 7400 Duo optical emission spectrometer. Samples sized $100 \times 10 \times 10$ mm were cut from the top and bottom parts of each casting and were then mounted to the chuck of a lathe. The samples were processed via a diamond turning tool at a low feed rate to obtain fine chips sized 3 mm. Chips of 1 g were calcined at 800°C for 2 h, followed by dissolution in a mixture of hydrochloric, hydrofluoric, and nitric acids using a microwave decomposition system at 180°C . The quantitative content of resulting solutions was analyzed for the major elements: Al, Si, Fe, Mn, Mg, and Er. Electron microscopic studies of the surface microstructure and the cross-section of the coated sample, as well as elemental analysis and fractographic studies of sample fractures after tensile tests were conducted using a Tescan MIRA 3 LMU scanning electron microscope equipped with an Oxford Instruments Ultim Max 40 energy-dispersive X-ray spectrometer. The alloy microstructure was studied through optical microscopy with the application of Metam LV 34 microscope (EqTRCS). The grain structure of the alloys was investigated through metallographic samples after electrolytic etching on an Olympus GX 71 (EqTRCS) optical microscope with an Olympus U-TP530 polarization filter. The investigation of the structure via transmission electron microscopy (TEM) methods was carried out using a microscope JEOL JEM-2100 microscope at an accelerating voltage of 300 kV on foils made via ion thinning using an Ion Slicer EM 09100IS system in a vacuum environment at a voltage of 6–8 kV and a tilt angle of $2\text{--}4^\circ$. Brinell hardness and Vickers hardness measurements of alloys were performed in this study. For the Brinell hardness experiment, a Metolab 703 hardness tester (EqTRCS) was used. A spherical indenter with a radius of 2.5 mm was used with a force of 62.5 kg and an exposure time of 10 s. For the Vickers hardness experiment, a Metolab 502 hardness tester (EqTRCS) was used. A spherical diamond indenter was used with a force of 50 g and an exposure time of 30 s. Tensile experiments were performed using an Instron 3369 (EqTRCS) universal electromechanical testing machine at a loading rate of 0.1 mm/min. For each group of alloys, 6 samples were made. Samples were cut from castings using electroerosion cutting and flat blades with a length and width of the working part of 25 and 6 mm, respectively; a thickness of 2 mm; and a rounding radius of 14 mm.

3. Results and Discussion

Figure 3 shows photographs of ErF_3 powder particles. The obtained powder consists of agglomerates of a submicron particle. The sizes of the fine particles are $10\text{--}100\ \mu\text{m}$, and the sizes of the large particles are $0.3\text{--}1.7$ mm. The surfaces of the large particles are covered with particles with a size of $46 \pm 31\ \mu\text{m}$ and submicron particles, as seen in Figure 3b.

The mechanical processing of the ErF_3 powder in a planetary mill for 20 min leads to the crushing of the main mass of large particles. The powder is completely sieved through a sieve with a cell size of $500\ \mu\text{m}$; the average particle size of erbium fluoride is $90 \pm 63\ \mu\text{m}$, excluding submicron particles (Figure 4a). Figure 4b shows that mechanical activation for 2 h allows us to obtain a homogeneous powder composed of erbium fluoride from individual particles of $0.8 \pm 0.3\ \mu\text{m}$ and their agglomerates up to $100\ \mu\text{m}$.

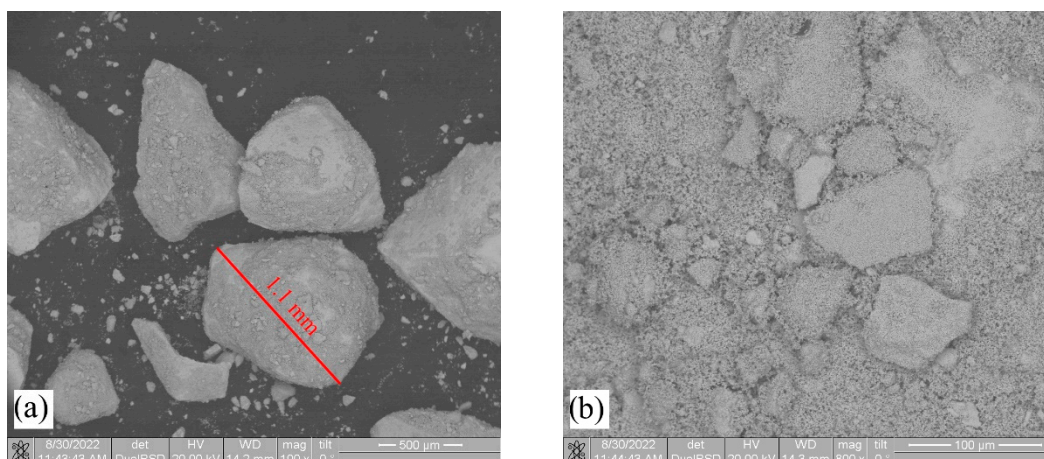


Figure 3. SEM micrographs of ErF_3 powder: ~ 1 mm particles (a) and submicron particles on the surface (b).

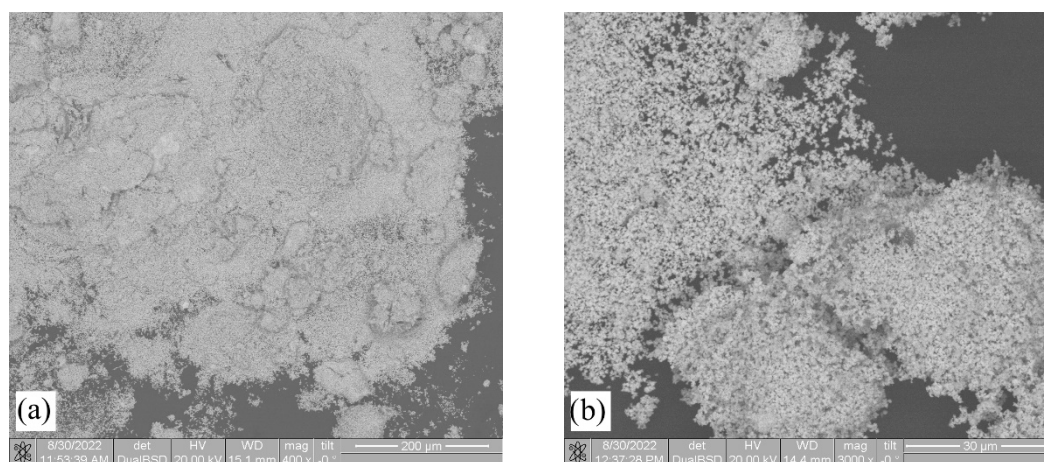


Figure 4. SEM micrographs of ErF_3 powder after 20 (a) and 120 (b) minutes of grinding in the planetary mill.

The diffraction pattern of the erbium fluoride powder after 120 min of crushing in a planetary mill is presented in Figure 5. The result of the decoding of the obtained diffractogram is presented in Table 1. The obtained powder exhibits an ErF_3 phase with a coherent scattering region size of 18 nm and a microstrain value of 2.2×10^{-3} .

Table 1. ErF_3 powder diffraction pattern interpretation results.

Phase	Volume Fraction, Mas. %	Lattice Parameters, Å	CSR Dimensions, nm	Microdistortions, $\Delta d/d$
ErF_3_{62}	100	a = 6.3437 b = 6.8863 c = 4.3935	18	2.2×10^{-3}

Note: CSR—coherent scattering regions.

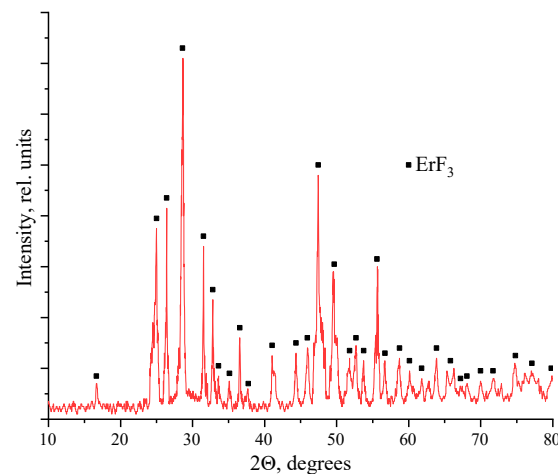


Figure 5. XRD pattern of ErF_3 powder after grinding in the planetary mill for 120 min.

Table 2 illustrates chemical composition in terms of Al, Si, Fe, Mn, Mg, and Er of the investigated alloys. The composition of the alloys is sufficiently homogeneous throughout the casting volume. Results show that the alloys correspond to the standard, and the erbium content in A359 + ErF_3 alloy is close to the calculated value (~ 0.75 wt%).

Table 2. Concentration range of Al, Si, Fe, Mn, Mg, and Er (wt%) of the experimental alloys.

	Al	Si	Fe	Mn	Mg	Er
A359	86.21–91.49	8.65–10.67	0.08–0.13	0.19–0.32	0.18–0.32	–
A359 + ErF_3	86.66–90.15	9.55–10.81	0.08–1.09	0.21–0.40	0.18–0.22	0.61–0.81

Figure 6a shows that the microstructure of the A359 alloy before heat treatment consists of an iron–manganese skeleton $\text{Al}_{15}(\text{FeMn})_3\text{Si}_2$ phase, a needle-like Al_5FeSi phase, an Al_2Cu (θ) phase, and primary crystals of $\text{Al}_{15}(\text{FeMnCr})_3\text{Si}_2$ phase in the obtained alloys. The Al_2Cu θ phase is represented by small spherical formations, which do not have a negative effect on the mechanical properties of the alloy [41]. In the Al–Si system alloys, a triple eutectic Al–Si– Al_5FeSi is formed in areas of high iron concentration [42]. The Al_5FeSi phase initiating cracks is represented as needles in the polished surface and as elongated plates in the volume [42]. The addition of manganese to Al–Si alloys allows for the binding of the needle-like phase Al_5FeSi into less negative skeletal formations (Chinese hieroglyphs) $\text{Al}_{15}(\text{FeMn})_3\text{Si}_2$ [41]. When the concentration of manganese exceeds 1% and iron exceeds 0.8%, primary crystals of $\text{Al}_{15}(\text{FeMn})_3\text{Si}_2$ may form [41]. Chromium or nickel are introduced as compensators for such compounds. Figure 6f shows that it does not prevent the formation of primary crystals of $\text{Al}_{15}(\text{FeMnCr})_3\text{Si}_2$ [43]. The resulting alloy showed a greater homogeneity of the distribution of iron-containing phases on the surface of grinds compared to the initial alloy, and practically no presence of the primary crystals of $\text{Al}_{15}(\text{FeMn})_3\text{Si}_2$ was detected.

SEM images of the A359 alloy are shown in Figure 6. The alloy consists of α -Al crystals (dark areas), silicon (gray areas), and intermetallic phases (light areas): Al_5FeSi , $\text{Al}_{15}(\text{FeMn})_3\text{Si}_2$, Al_2Cu , and $\text{Al}_{15}(\text{FeMnCr})_3\text{Si}_2$.

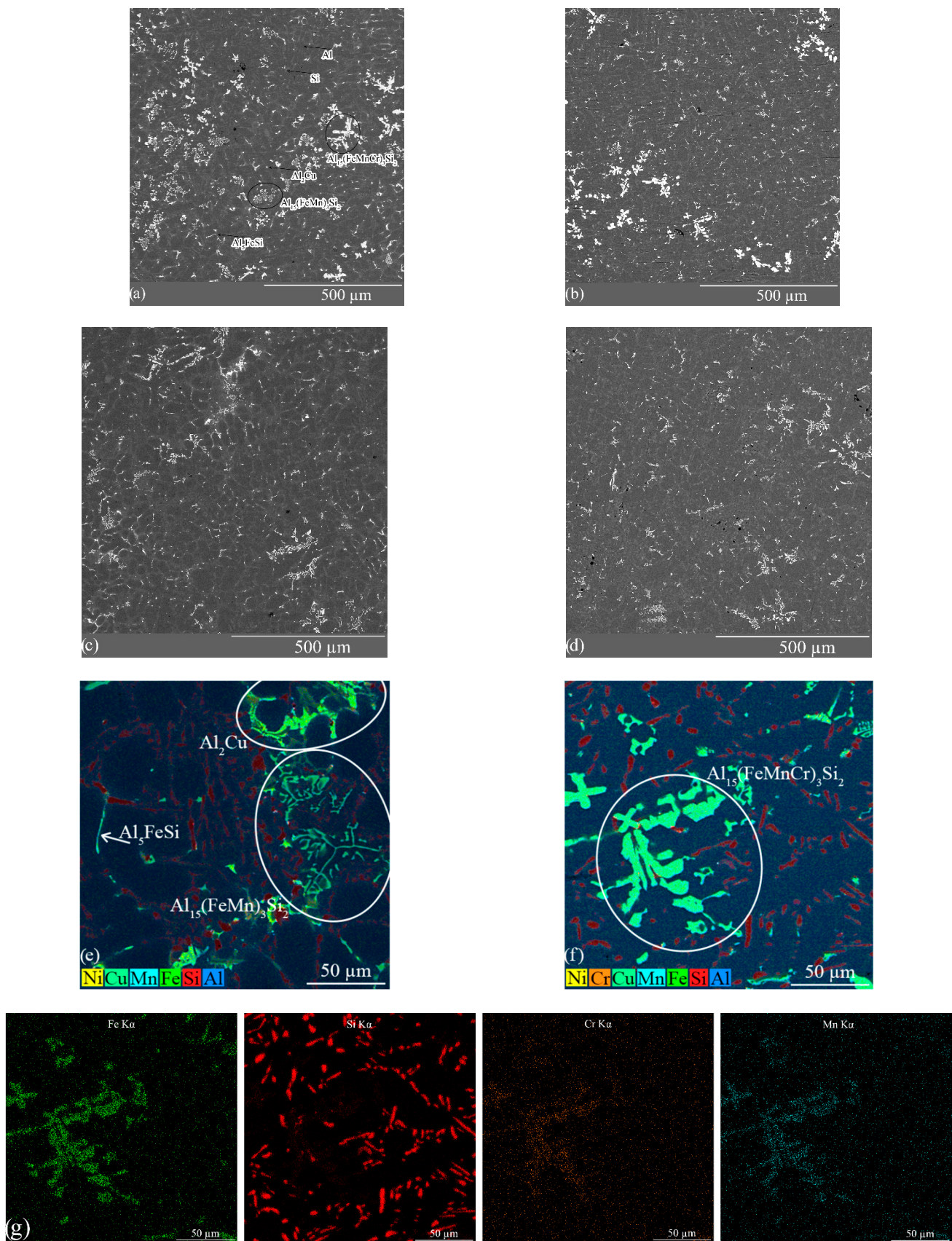


Figure 6. SEM micrographs of alloys before and after heat treatment: A359 (a); A359 + (T6) (b); A359 + ErF₃ (c); A359 + ErF₃ + (T6) (d). Results of element mapping of A359 alloy (e,f); mapping by individual elements (g).

The optical micrographs of the alloys (Figure 7) show the α -Al grains (light areas) and β -phase (dark) silicon. The $\text{Al}_{15}(\text{FeMn})_3\text{Si}_2$ skeletal phase and primary crystals of $\text{Al}_{15}(\text{FeMnCr})_3\text{Si}_2$ are also detected in the plane of metallographic grinds. In view of the absence of a pronounced dendritic structure of the obtained alloys, it is difficult to assess the effect of ErF_3 particles on the sizes of α -Al.

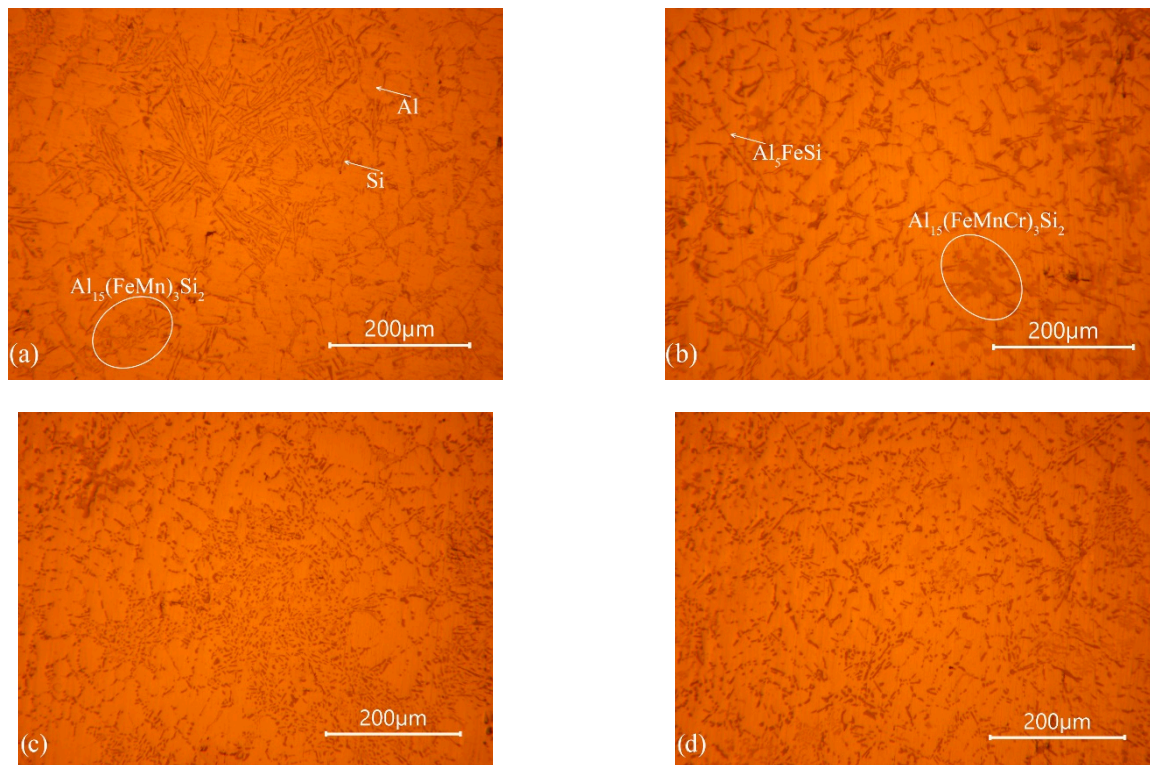


Figure 7. Optical micrographs of A359 and A359 + ErF_3 alloys before and after heat treatment: A359 (a); A359 + ErF_3 (b); A359 + (T6) (c); A359 + ErF_3 + (T6) (d).

In the plane of thin sections of alloys before heat treatment, the eutectic silicon phase occupies 20–30% of the section area. The alloy without the addition of erbium trifluoride shown in Figure 7a. In the alloy there are areas of accumulation of mostly needle-shaped β -phase silicon with linear size up to 100 μm . The introduction of erbium trifluoride particles shown in Figure 7b leads to the reduction in size of the β -phase with linear dimensions up to 30 μm and some rounding of the ends. The β -phase acquires a globular shape, and its sizes are reduced to $8 \pm 5 \mu\text{m}$ for alloys of both groups as a result of heat treatment (T6).

Figure 8 shows the grain structure of the studied alloys as a result of electrolytic etching of metallographic specimen. It is known that during casting in coquille the crystallization of the melt starts on the walls of the mold. The average grain size of α -Al was $315 \pm 131 \mu\text{m}$ in the areas of the A359 alloy castings bordering the coquille. It was found that in similar areas of A359 + ErF_3 alloy castings the average grain size of α -Al was $304 \pm 136 \mu\text{m}$. Thus, the introduction of ErF_3 particles into the A359 alloy did not lead to a change in the average grain size in the casting sections bordering the coquille. The maximum grain size of the studied areas of the A359 alloy castings was achieved in the central part, where the average grain size of α -Al was $518 \pm 215 \mu\text{m}$. In similar areas of A359 + ErF_3 alloy castings, the average grain size of α -Al was $412 \pm 164 \mu\text{m}$. Thus, the introduction of ErF_3 particles into the A359 alloy led to a reduction in the average grain size of α -Al in the central part of the casting.

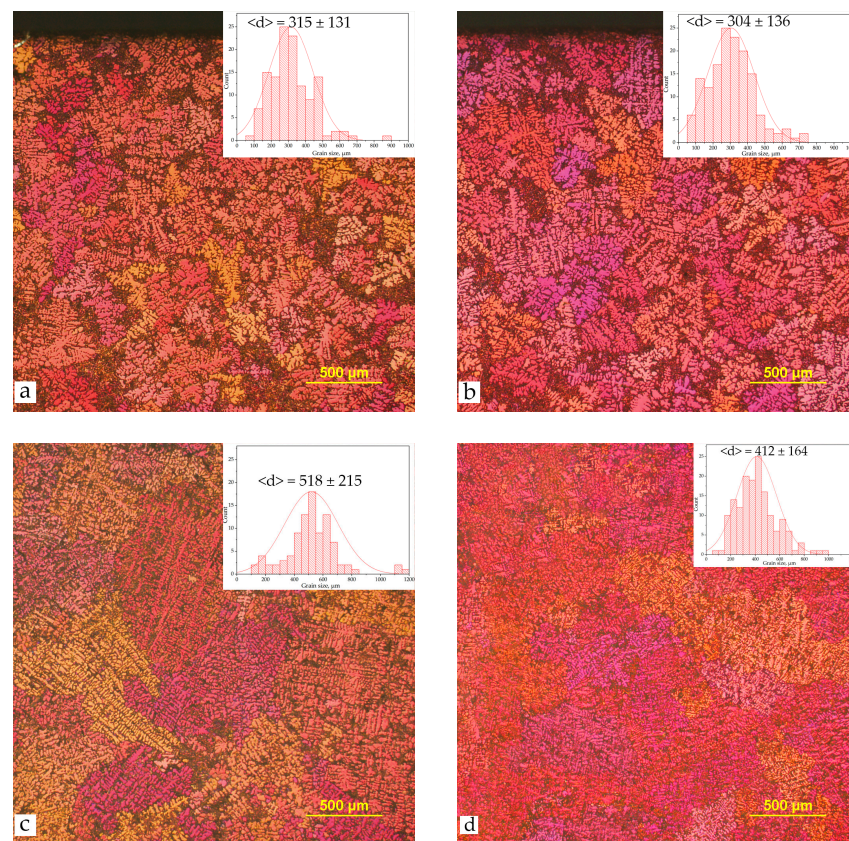


Figure 8. Optical micrographs of A359 (a,c) and A359 + ErF₃ (b,d) alloys: photo of the area in the center of the casting (c,d) and the area on the border with the coquille (a,b).

Inoculant particles should have a high affinity for lattice parameters with the crystallizing metal [44] to act as a nucleation site for the effective refinement of the grain structure of the matrix alloy. Aluminum and silicon have a face-centered cubic lattice, while erbium fluoride has an orthorhombic lattice. Additionally, another mechanism of particle influence on the alloy structure is known when particles in contact with each other are located along the boundaries of the growing grain [45].

Generally, during the crystallization of α -Al grains, the dominant direction of the propagation of the crystallization front is formed, which can displace intermetallic phases suspended in the melt from the crystallization region. This effect leads to the formation of clusters of intermetallic phases, which form areas of reduced strength in the resulting castings. In turn, submicro- and nanoparticles in the melt can encircle the growing grains, forming a barrier between the growing aluminum grain and the feeding melt. This inhibits the crystallization front and promotes the formation of grain nuclei outside the main crystallization front. Summarizing the results of the study of the microstructure of the obtained alloys: based on the difference in the crystal lattices of Al and ErF₃, ErF₃ particles cannot be effective centers of crystallization, while a high uniformity of the structure of alloys containing ErF₃ particles is noted. It can be concluded that the contribution of ErF₃ particles to the structure of Al-Si alloys is to reduce the formation of clusters of iron phases and eutectic lamellar silicon. Schematically, the implementation of this mechanism is shown in Figure 9.

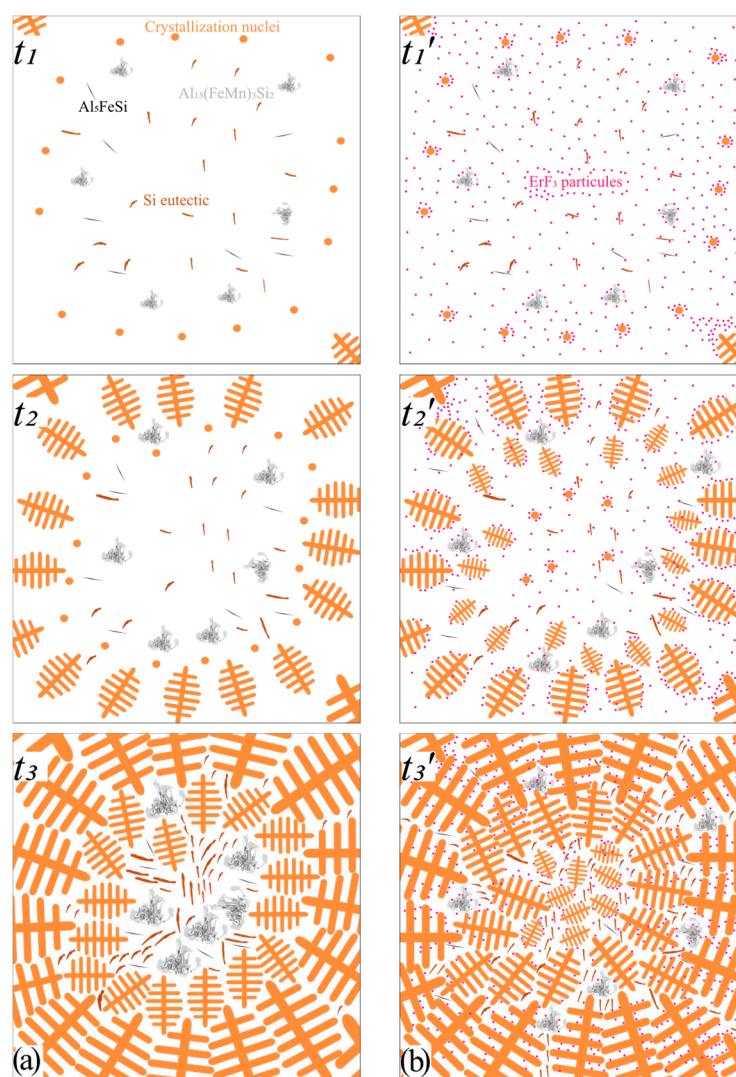


Figure 9. Scheme of the effect of ErF_3 particles on the structure of Al–Si alloys: alloy without particles at timepoints t_1 , t_2 , and t_3 (a) and Al–Si + ErF_3 alloy at timepoints t_1' , t_2' , and t_3' (b).

As can be seen from Figure 10, ErF_3 particles in the alloy are on the grain boundaries of α -Al. This fact may be an indirect confirmation of the implementation of the mechanism of holding back the crystallization front by ErF_3 particles. The results of the EDX analysis of the area shown in Figure 10a are presented in Table 3.

Table 3. Energy dispersive X-ray analysis of the Figures 10a, 13b, and 14a.

Label	Al	Fe	Mn	Cr	Si	Er	F	Mg	C	O	Cu
1	63.72	1.4	0	0	4.9	12.7	8.88	2.2	1.13	4.17	0.9
2	65.57	13.76	3.94	1.60	12.31	0	0.24	0.14	0.85	0.42	1.17
3	13.04	0.5	0	0	2.18	71.76	6.56	0.13	1.29	4.54	0
4	9.77	0.56	0	0	1.21	64.39	13.69	4.95	1.28	4.15	0

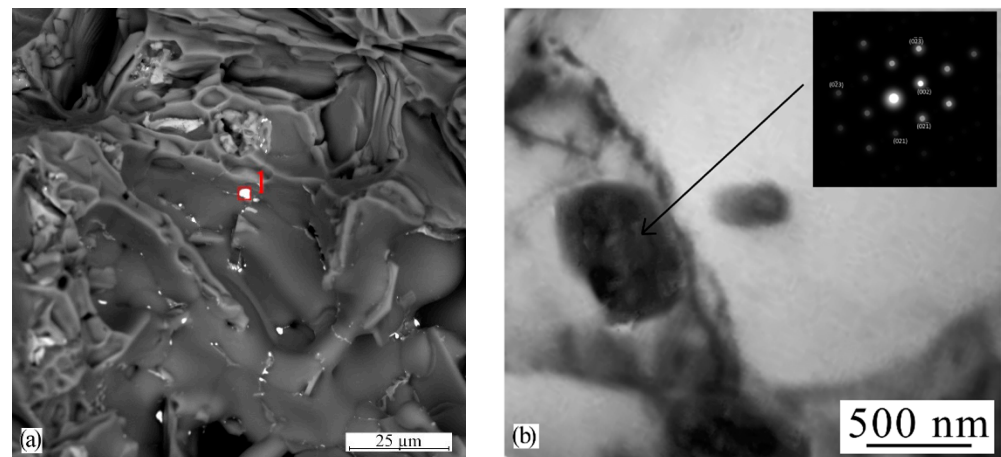


Figure 10. ErF_3 particles on the grain boundaries of alloy A359: an SEM image of the fracture surface (a) and a TEM image of the alloy (b).

The density of the A359 alloy is $2.73 \pm 0.01 \text{ g/cm}^3$. The alloy with erbium fluoride is less homogeneous in density, measuring $2.72 \pm 0.03 \text{ g/cm}^3$. Figure 6d shows that the reason for this density is the presence of more pores in the alloy volume. The hardness and microhardness values of the studied alloys are presented in Table 4. It can be seen that the hardness value of the A359 alloy increases from 86.3 to 118.6 HB as a result of heat treatment (T6) and does not depend on the addition of ErF_3 particles. In the A359 alloy, the microhardness value of the $\text{Al}_{15}(\text{FeMn})_3\text{Si}_2$ phase is 107.6 HV. The addition of ErF_3 particles to the A359 alloy provides an increase in the $\text{Al}_{15}(\text{FeMn})_3\text{Si}_2$ phase microhardness from 107.6 to 143.9 HV. At the same time, the heat treatment of the alloy increases the microhardness values of the $\text{Al}_{15}(\text{FeMn})_3\text{Si}_2$ phase and reduces the particles contribution to its increase. This dependence correlates with the noted positive effect of ErF_3 particles on the morphology of eutectic silicon before the alloy heat treatment.

Table 4. Hardness and microhardness values of the phases of the investigated alloys.

Alloy	HB	HV(Al)	HV(Si)	HV($\beta(\text{Al}_5)$)	HV($\alpha_m(\text{Al}_{15})$)	HV($\alpha_m(\text{Al}_{15}) + \text{Cr}$)
A359	86.3 ± 2.6	81.8 ± 6	92.7 ± 12	98.6 ± 6	107.6 ± 23	230 ± 98
A359 + ErF_3	84.9 ± 4.2	83.5 ± 6	95.3 ± 8	95.4 ± 6	143.9 ± 29	245 ± 68
A359 (T6)	118.6 ± 3.5	117.8 ± 6	134.7 ± 18	128 ± 8	153.2 ± 14	181 ± 68
A359 + ErF_3 (T6)	118.1 ± 4.5	117.3 ± 7	135 ± 13	123 ± 8	163 ± 14	190 ± 55

Note: HB—Brinell hardness; HV—Vickers microhardness of phases; $\beta(\text{Al}_5)$ — Al_5FeSi ; $\alpha_m(\text{Al}_{15})$ — $\text{Al}_{15}(\text{FeMn})_3\text{Si}_2$; $\alpha_m(\text{Al}_{15}) + \text{Cr}$ — $\text{Al}_{15}(\text{FeMnCr})_3\text{Si}_2$.

Figure 11 shows typical stress–strain curves of A359 and A359 + ErF_3 alloys before and after heat treatment. The alloys exhibit typical Al–Si system alloys deformation behavior: elastic deformation zone prevails over the plastic flow zone, no deformation localization zone is present, and crack propagation work is minimal. Heat treatment according to the (T6) regime provides an increase in the maximum stresses of the elastic zone of the alloys while reducing their plasticity properties. It was found that the effect of erbium fluoride particles on the deformation behavior of the A359 alloy varied depending on the structural state of the alloy. The particles in the cast alloy provided a positive effect on the stress–strain state in the elastic deformation zone and provide an increase in plasticity properties. The particles in the alloy after heat treatment provided a significant increase in elastic stresses with a small contribution to the plastic flow work of the material.

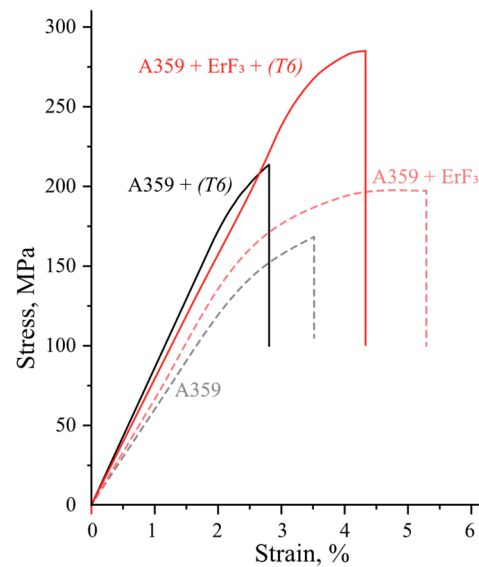


Figure 11. Load diagrams of the alloys before and after heat treatment.

Table 5 shows the mechanical properties of the alloys. According to the results obtained, there is a positive trend in the increase in strength properties of the alloy before and after heat treatment as a result of the addition of particles. In the A359 alloy, in its cast state, the addition of 1 wt% ErF_3 leads to an increase in the ultimate strength from 168 to 195 MPa and the relative elongation from 0.7 to 2.3%. In a heat-treated state, the addition of 1 wt% ErF_3 to alloy A359 provides an increase in the yield strength from 197 to 267 MPa and in the tensile strength from 213 to 286 MPa and increases the maximum strain for failure from 2.5 to 4.3%. The increase in the yield strength values of the A359 alloy can be associated with the refinement of the average grain size (Figure 8), according to the Hall–Petch law [5]. In turn, the increase in the ductility of A359 + ErF_3 alloy can be realized by reducing the clustering of the iron phase (Figure 7) embrittlement of Al–Si alloys.

Table 5. Mechanical properties of alloys.

Alloy	State	$\sigma_{0.2}$, MPa	σ_B , MPa	ϵ_{\max} , %	δ , %
A359	As-cast	142 ± 7	168 ± 11	3.5 ± 0.8	0.7 ± 0.2
A359 + ErF_3		162 ± 8	195 ± 13	4.9 ± 1	2.3 ± 0.3
A359	(T6)	197 ± 6	213 ± 13	2.5 ± 0.4	0.3 ± 0.1
A359 + ErF_3		267 ± 7	286 ± 13	4.3 ± 0.4	0.8 ± 0.2

Note: $\sigma_{0.2}$ —yield strength; σ_B —ultimate tensile strength; ϵ_{\max} —maximum deformations before failure; δ —elongation.

Figure 12 shows the fracture surface of the A359 alloys before and after heat treatment. It was found that a decrease in maximum deformation does not affect the nature of the fracture. The fracture surface is oriented perpendicularly to the axis of tension, and the surface morphology is characterized by homogeneous cleavage.

Figure 13b shows that the surface of fracture of the A359 alloy is dotted with cracked intermetallics $\text{Al}_{15}(\text{FeMn})_3\text{Si}$ and $\text{Al}_{15}(\text{FeMnCr})_3\text{Si}$ (Table 3). The introduction of erbium fluoride does not affect the fracture behavior of the A359 alloy. The fracture occurs through the mechanism of the shear facet with the formation of a stream-like microrelief. This is probably due to the iron-containing intermetallics acting as stress concentrators, and upon reaching the allowable load, they crack, followed by the fracture of aluminum grains through the transcrystalline mechanism, which is demonstrated in Figure 13c.

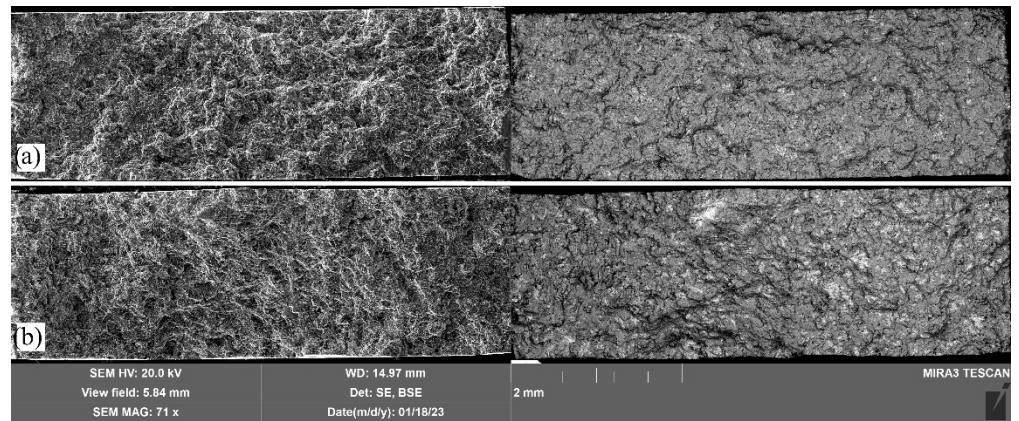


Figure 12. SEM micrographs of the A359 alloy fracture surface before (a) and after (b) heat treatment for detecting secondary (left images) and backscattered electrons (right images).

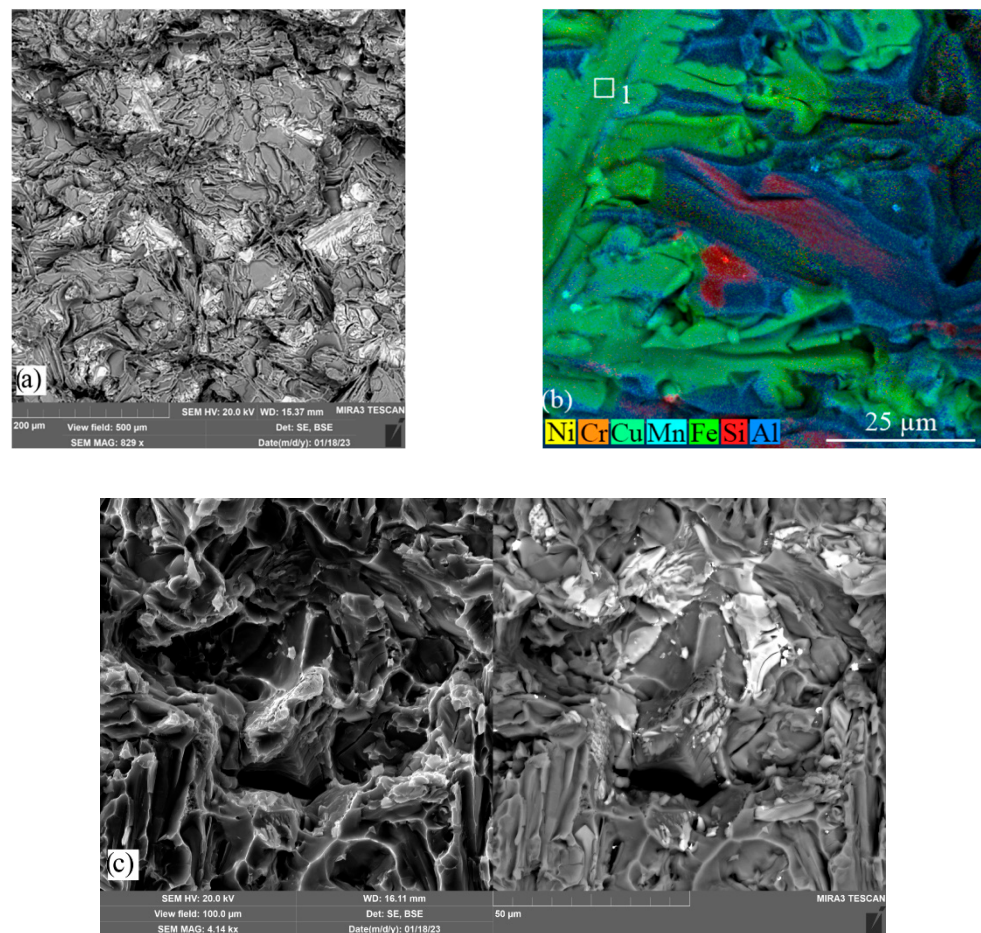


Figure 13. SEM micrographs of the alloys fracture surface: surface with ferrous intermetallics (a); mapping of the area with the cracked $\text{Al}_{15}(\text{FeMnCr})_3\text{Si}$ phase (b); transcrystalline cracking of aluminum grains (c).

Admittedly, to create metal-matrix composites with enhanced strength properties, it is necessary to have a uniform distribution of reinforcing particles [30]. Figure 14a shows that there are areas of accumulation of erbium fluoride on the surfaces of fracture of A359 + ErF_3 alloy samples with reduced strength properties. Thus, the introduction of erbium fluoride with preliminary deagglomeration in aluminum micropowder and mechanical mixing

using a special mixer does not provide the uniform distribution of particles in the alloy matrix. There are approaches to using ultrasound treatment of the melt and vibrational impact during casting to deagglomerate ex situ-introduced particles and increase their wettability. The influence of ErF_3 particles under the complex action of external fields on the structure and the physico-mechanical properties of the A359 alloy will be further studied in the future.

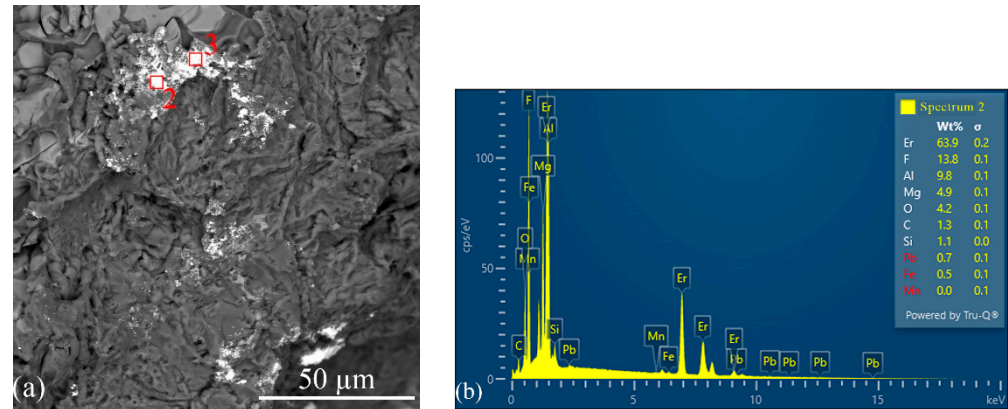


Figure 14. The agglomeration of ErF_3 particles on the A359 + ErF_3 alloy fracture surface after tensile test (a) and EDX spectrum from point 2 (b).

4. Conclusions

The introduction of ErF_3 particles results in less accumulation of intermetallic phases and reduces the linear sizes of eutectic Si particles by $\sim 70\%$ with the formation of a larger rounding radius on the boundaries. As a result of the heat treatment of the studied alloys, according to the (T6) mode, the eutectic Si particles acquire a globular shape, and their sizes are reduced to $8 \pm 5 \mu\text{m}$ for the alloys of both groups. It was found that the modifying effect of ErF_3 particles on the structure of aluminum–silicon alloys is realized through the mechanism of crystallization front inhibition; it weakly affects the indices of the average size of dendritic cells and is manifested to reduce the formation of clusters of iron phases and eutectic lamellar silicon.

It was found that the introduction of 1 wt% ErF_3 does not affect the hardness values of the alloy and the microhardness of the Al, Si, and Al_5FeSi phases and leads to an increase in the microhardness of the $\text{Al}_{15}(\text{FeMn})_3\text{Si}_2$ phase by 34% and the $\text{Al}_{15}(\text{FeMnCr})_3\text{Si}_2$ phase by 7%. It was found that the addition of 1 wt% ErF_3 to the A359 alloy leads to an increase in the values of yield strength from 142 to 162 MPa and ultimate tensile strength from 168 to 195 MPa. Heat treatment, according to the (T6) mode, leads to a decrease in ductility by 57% and 65% for the A359 and A359 + ErF_3 alloys, respectively. However, the values of yield strength and ultimate tensile strength increase by 39% and 27%, respectively, in the A359 alloy and by 65% and 47%, respectively, in the A359 + ErF_3 alloy. The introduction of erbium fluoride does not affect the character of the destruction of the A359 alloy. The destruction occurs via the shear facet mechanism with the formation of a streaky microrelief. Iron intermetallics act as stress concentrators, the appearance of which initiates the sample cracking via the transgranular mechanism. It was noted that the improvement in the strength properties of the A359 alloy by adding 1 wt% of ErF_3 is combined with the negative effect of its agglomerates and clusters, which cannot be eliminated through preliminary deagglomeration in aluminum micropowder and melt processing using a mechanical mixing device. Thus, by ensuring the uniform distribution of ErF_3 particles throughout the material volume, a significant increase in the strength properties of the original alloy can be expected.

Author Contributions: Investigation and visualization, N.K. and V.V.; writing—original draft preparation, N.K., V.V. and M.S.; formal analysis, M.S.; writing—review, data curation, and editing, A.K.;

methodology, validation, conceptualization, project administration, and funding acquisition I.Z., A.V. and S.V. All authors have read and agreed to the published version of the manuscript.

Funding: This work was carried out with financial support from the Ministry of Education and Science of the Russian Federation (state assignment no. FSWM-2020-0028).

Data Availability Statement: Not applicable.

Acknowledgments: The research was carried out with the equipment of Tomsk Regional Core Shared Research Facilities Center of National Research Tomsk State University. The Center is supported by the Ministry of Science and Higher Education of the Russian Federation, grant no. 075-15-2021-693 (no. 13.RFC.21.0012).

Conflicts of Interest: The authors declare no conflict of interest.

References

1. Zhang, L.; Eskin, D.G.; Miroux, A.; Katgerman, L. Formation of Microstructure in Al-Si Alloys Under Ultrasonic Melt Treatment. *Light Met.* **2012**, *2012*, 999–1004. [[CrossRef](#)]
2. Zakharov, V.V. Effect of Scandium on the Structure and Properties of Aluminum Alloys. *Met. Sci. Heat Treat.* **2003**, *45*, 246–253. [[CrossRef](#)]
3. Zhou, S.; Zhang, Z.; Li, M.; Pan, D.; Su, H.; Du, X.; Li, P.; Wu, Y. Effect of Sc on microstructure and mechanical properties of as-cast Al-Mg alloys. *Mater. Des.* **2016**, *90*, 1077–1084. [[CrossRef](#)]
4. Zhou, S.; Zhang, Z.; Li, M.; Pan, D.; Su, H.; Du, X.; Li, P.; Wu, Y. Correlative characterization of primary particles formed in as-cast Al-Mg alloy containing a high level of Sc. *Mater. Charact.* **2016**, *118*, 85–91. [[CrossRef](#)]
5. Hansen, N. Hall-Petch relation and boundary strengthening. *Scr. Mater.* **2004**, *51*, 801–806. [[CrossRef](#)]
6. Zhang, Z.; Chen, D.L. Contribution of Orowan strengthening effect in particulate-reinforced metal matrix nanocomposites. *Mater. Sci. Eng. A* **2008**, *483*, 148–152. [[CrossRef](#)]
7. Buranova, Y.; Kulitskiy, V.; Peterlechner, M.; Mogucheva, A.; Kaibyshev, R.; Divinski, S.; Wilde, G. Al₃(Sc,Zr)-based precipitates in Al-Mg alloy: Effect of severe deformation. *Acta Mater.* **2017**, *124*, 210–224. [[CrossRef](#)]
8. Sitdikov, O.; Garipova, R.; Avtokratova, E.; Mukhametdinova, O.; Markushev, M. Effect of temperature of isothermal multidirectional forging on microstructure development in the Al-Mg alloy with nano-size aluminides of Sc and Zr. *J. Alloys Compd.* **2018**, *746*, 520–531. [[CrossRef](#)]
9. Tang, L.; Peng, X.; Huang, J.; Ma, A.; Deng, Y.; Xu, G. Microstructure and mechanical properties of severely deformed Al-Mg-Sc-Zr alloy and their evolution during annealing. *Mater. Sci. Eng. A* **2018**, *754*, 295–308. [[CrossRef](#)]
10. Jiang, F.; Zhou, J.; Huang, H.; Qu, J. Characterisation of microstructure and mechanical properties in Al-Mg alloy with addition of Sc and Zr. *Mater. Res. Innov.* **2014**, *18*, S4-228–S4-234. [[CrossRef](#)]
11. Li, M.; Pan, Q.; Shi, Y.; Sun, X.; Xiang, H. High strain rate superplasticity in an Al-Mg-Sc-Zr alloy processed via simple rolling. *Mater. Sci. Eng. A* **2017**, *687*, 298–305. [[CrossRef](#)]
12. Malopheyev, S.; Kulitskiy, V.; Mironov, S.; Zhemchuzhnikova, D.; Kaibyshev, R. Friction-stir welding of an Al-Mg-Sc-Zr alloy in as-fabricated and work-hardened conditions. *Mater. Sci. Eng. A* **2014**, *600*, 159–170. [[CrossRef](#)]
13. Pan, D.; Zhou, S.; Zhang, Z.; Li, M.; Wu, Y. Effects of Sc(Zr) on the microstructure and mechanical properties of as-cast Al-Mg alloys. *Mater. Sci. Technol.* **2017**, *33*, 751–757. [[CrossRef](#)]
14. Xu, C.; Xiao, W.; Zheng, R.; Hanada, S.; Yamagata, H.; Ma, C. The synergic effects of Sc and Zr on the microstructure and mechanical properties of Al-Si-Mg alloy. *Mater. Des.* **2015**, *88*, 485–492. [[CrossRef](#)]
15. Zhang, W.; Liu, Y.; Yang, J.; Dang, J.; Xu, H.; Du, Z. Effects of Sc content on the microstructure of As-Cast Al-7wt.% Si alloys. *Mater. Charact.* **2012**, *66*, 104–110. [[CrossRef](#)]
16. Kim, M.; Hong, Y.; Cho, H. The effects of Sc on the microstructure and mechanical properties of hypo-eutectic Al-Si alloys. *Met. Mater. Int.* **2004**, *10*, 513–520. [[CrossRef](#)]
17. Srinivas, D.; Gowrishankar, M.C.; Hiremath, P.; Sharma, S.; Shettar, M.; PK, J. Influence of various trace metallic additions and reinforcements on A319 and A356 alloys—A review. *Cogent Eng.* **2022**, *9*, 2007746. [[CrossRef](#)]
18. Muhammad, A.; Xu, C.; Xuejiao, W.; Hanada, S.; Yamagata, H.; Hao, L.; Chaoli, M. High strength aluminum cast alloy: A Sc modification of a standard Al-Si-Mg cast alloy. *Mater. Sci. Eng. A* **2014**, *604*, 122–126. [[CrossRef](#)]
19. Pramod, S.; Ravikiran; Rao, A.P.; Murty, B.; Bakshi, S.R. Effect of Sc addition and T6 aging treatment on the microstructure modification and mechanical properties of A356 alloy. *Mater. Sci. Eng. A* **2016**, *674*, 438–450. [[CrossRef](#)]
20. Xu, C.; Xiao, W.; Hanada, S.; Yamagata, H.; Ma, C. The effect of scandium addition on microstructure and mechanical properties of Al-Si-Mg alloy: A multi-refinement modifier. *Mater. Charact.* **2015**, *110*, 160–169. [[CrossRef](#)]
21. Qian, H.; Zhu, D.; Hu, C.; Jiang, X. Effects of Zr Additive on Microstructure, Mechanical Properties, and Fractography of Al-Si Alloy. *Metals* **2018**, *8*, 124. [[CrossRef](#)]
22. Zuo, M.; Jiang, K.; Liu, X. Refinement of hypereutectic Al-Si alloy by a new Al-Zr-P master alloy. *J. Alloys Compd.* **2010**, *503*, L26–L30. [[CrossRef](#)]
23. Czerwinski, F. Cerium in aluminum alloys. *J. Mater. Sci.* **2020**, *55*, 24–72. [[CrossRef](#)]

24. Ahmad, R.; Asmael, M.B.A. Influence of Lanthanum on Solidification, Microstructure, and Mechanical Properties of Eutectic Al-Si Piston Alloy. *J. Mater. Eng. Perform.* **2016**, *25*, 2799–2813. [CrossRef]
25. Voron, M.M.; Pruss, M.F.; Byba, O.Y. Microalloying and Modification of Cast Aluminum Alloys for Increasing their Level of Exploitation Properties at Elevated Temperatures. A Review. *Foundry Process. Technol. Mater.* **2021**, *145*, 61–68. [CrossRef]
26. Nogita, K.; McDonald, S.D.; Dahle, A.K. Eutectic Modification of Al-Si Alloys with Rare Earth Metals. *Mater. Trans.* **2004**, *45*, 323–326. [CrossRef]
27. HosseiniFar, M.; Malakhov, D.V. Effect of Ce and La on microstructure and properties of a 6xxx series type aluminum alloy. *J. Mater. Sci.* **2008**, *43*, 7157–7164. [CrossRef]
28. Pourbahari, B.; Emamy, M.; Lotfpour, M.; Allameh, S.H. Effects of La intermetallics on the structure and tensile properties of thin section gravity die-cast A357 Al alloy. In Proceedings of the International Conference on Chemical, Metallurgy and Environmental Engineering (ICMAEE '15), Phuket, Thailand, 20–21 December 2015; pp. 296–303. [CrossRef]
29. Lin, S.; Nie, Z.; Huang, H.; Li, B. Annealing behavior of a modified 5083 aluminum alloy. *Mater. Des.* **2010**, *31*, 1607–1612. [CrossRef]
30. Khrustalyov, A.P.; Kozulin, A.A.; Zhukov, I.A.; Nikitin, P.Y.; Sachkov, V.I.; Vorozhtsov, A.B. Effect of Al₃Er Particles on the Structure, Mechanical Properties, and Fracture of AA5056 Alloy After Casting and Deformation Treatment. *JOM* **2021**, *73*, 3858–3865. [CrossRef]
31. Singh, Y. *Rare Earth Element Resources: Indian Context*; Springer: Berlin/Heidelberg, Germany, 2020; p. 388. [CrossRef]
32. Mathur, V.; Subramanya, R.P.B.; Manjunath, P.G.C.; Shettigar, A.K. Reinforcement of titanium dioxide nanoparticles in aluminium alloy AA 5052 through friction stir process. *Adv. Mater. Process. Technol.* **2019**, *5*, 329–337. [CrossRef]
33. Lekatou, A.; Karantzalis, A.; Evangelou, A.; Gousia, V.; Kaptay, G.; Gácsi, Z.; Baumli, P.; Simon, A. Aluminium reinforced by WC and TiC nanoparticles (ex-situ) and aluminide particles (in-situ): Microstructure, wear and corrosion behaviour. *Mater. Des.* **2015**, *65*, 1121–1135. [CrossRef]
34. Chen, B.; Zhou, X.; Zhang, B.; Kondoh, K.; Li, J.; Qian, M. Microstructure, tensile properties and deformation behaviors of aluminium metal matrix composites co-reinforced by ex-situ carbon nanotubes and in-situ alumina nanoparticles. *Mater. Sci. Eng. A* **2020**, *795*, 139930. [CrossRef]
35. Mousavian, R.T.; Khosroshahi, R.A.; Yazdani, S.; Brabazon, D.; Boostani, A. Fabrication of aluminum matrix composites reinforced with nano- to micrometer-sized SiC particles. *Mater. Des.* **2016**, *89*, 58–70. [CrossRef]
36. Vorozhtsov, S.; Zhukov, I.; Promakhov, V.; Naydenkin, E.; Khrustalyov, A.; Vorozhtsov, A. The Influence of ScF₃ Nanoparticles on the Physical and Mechanical Properties of New Metal Matrix Composites Based on A356 Aluminum Alloy. *JOM* **2016**, *68*, 3101–3106. [CrossRef]
37. Ko, J.M.; Durbin, S.D.; Fukuda, T.; Inaba, K. Nonisomorphic ErF₃ layers on Si(111) substrates grown by molecular beam epitaxy. *J. Vac. Sci. Technol. A Vac. Surf. Film.* **2000**, *18*, 922–926. [CrossRef]
38. Kim, Y.-M.; Choi, S.-W.; Hong, S.-K. Influence of Si content on thermal expansion characteristic of Al-Si alloys. *Mater. Sci. Technol.* **2020**, *36*, 709–716. [CrossRef]
39. Vorozhtsov, S.; Minkov, L.; Dammer, V.; Khrustalyov, A.; Zhukov, I.; Promakhov, V.; Vorozhtsov, A.; Khmeleva, M. Ex Situ Introduction and Distribution of Nonmetallic Particles in Aluminum Melt: Modeling and Experiment. *JOM* **2017**, *69*, 2653–2657. [CrossRef]
40. Elibrary. Science Digital Library. Available online: <https://www.elibrary.ru/item.asp?id=43877731> (accessed on 15 June 2023).
41. Wang, E.; Hui, X.; Wang, S.; Zhao, Y.; Chen, G. Improved mechanical properties in cast Al-Si alloys by combined alloying of Fe and Cu. *Mater. Sci. Eng. A* **2010**, *527*, 7878–7884. [CrossRef]
42. Dinnis, C.M.; Taylor, J.A.; Dahle, A.K. As-cast morphology of iron-intermetallics in Al-Si foundry alloys. *Scr. Mater.* **2005**, *53*, 955–958. [CrossRef]
43. Khan, M.; Das, A.; Li, Z.; Kotadia, H. Effects of Fe, Mn, chemical grain refinement and cooling rate on the evolution of Fe intermetallics in a model 6082 Al-alloy. *Intermetallics* **2021**, *132*, 107132. [CrossRef]
44. Liu, B.; Ma, C.; Li, L.; Yang, C.; Yu, N.; Wang, W.; Gao, T. Morphologies and Compositions of α -Al₁₅Fe₃Si₂-Type Intermetallics in Al-Si-Fe-Mn-Cr Alloys. *Int. J. Met.* **2023**, *71*, 1156–1164. [CrossRef]
45. Khrustalyov, A.P.; Akhmadieva, A.; Monogenov, A.N.; Zhukov, I.A.; Marchenko, E.S.; Vorozhtsov, A.B. Study of the Effect of Diamond Nanoparticles on the Structure and Mechanical Properties of the Medical Mg-Ca-Zn Magnesium Alloy. *Metals* **2022**, *12*, 206. [CrossRef]

Disclaimer/Publisher's Note: The statements, opinions and data contained in all publications are solely those of the individual author(s) and contributor(s) and not of MDPI and/or the editor(s). MDPI and/or the editor(s) disclaim responsibility for any injury to people or property resulting from any ideas, methods, instructions or products referred to in the content.